# LANGMUIR

pubs.acs.org/Langmuir Article

# Droplet Evaporation Dynamics of Low Surface Tension Fluids Using the Steady Method

A. Alperen Günay,\* Marisa Gnadt, Soumyadip Sett, Hamed Vahabi, Arun K. Kota, and Nenad Miljkovic\*



Cite This: Langmuir 2020, 36, 13860-13871



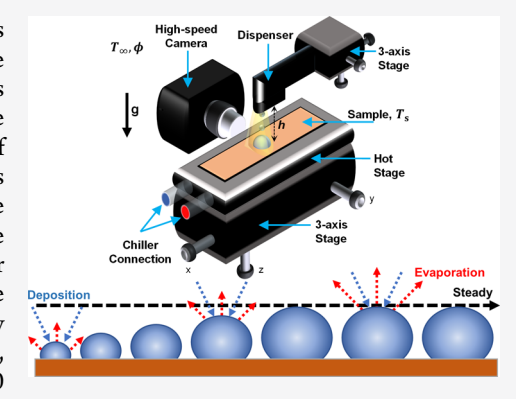
**ACCESS** 

Metrics & More

Article Recommendations

Supporting Information

**ABSTRACT:** Droplet evaporation governs many heat- and mass-transfer processes germane in nature and industry. In the past 3 centuries, transient techniques have been developed to characterize the evaporation of sessile droplets. These methods have difficulty in reconciling transient effects induced by the droplet shape and size changes during evaporation. Furthermore, investigation of evaporation of microdroplets residing on wetting substrates, or fluids having low surface tensions (<30 mN/m), is difficult to perform using established approaches. Here, we use the steady method to study the microdroplet evaporation dynamics of low surface tension liquids. We start by employing the steady method to benchmark with water droplets having base radii ( $20 \le R_b \le 260 \ \mu\text{m}$ ), apparent advancing contact angle ( $45^\circ \le \theta_{a,app} \le 162^\circ$ ), surface temperature ( $30 < T_s < 60 \ ^\circ\text{C}$ ), and relative humidity ( $40\% < \phi < 60\%$ ). Following validation, evaporation of ethanol ( $\approx 22 \ \text{mN/m}$ ), hexane ( $\approx 18 \ \text{mN/m}$ ), and dodecane ( $\approx 25 \ \text{mN/m}$ ) were studied for  $90 \le R_b \le 400 \ \mu\text{m}$  and  $10 < T_s < 25 \ ^\circ\text{C}$ . We elucidate the mechanisms governing the observed



behavior using heat and mass transport scaling analysis during evaporation, demonstrating our steady technique to be particularly advantageous for microdroplets, where Marangoni and buoyant forces are negligible. Our work not only elucidates the droplet evaporation mechanisms of low surface tension liquids but also demonstrates the steady method as a means to study phase change processes.

#### ■ INTRODUCTION

Droplet evaporation governs several industrial processes such as liquid hydrocarbon combustion<sup>1-4</sup> and phase change heat transfer. 5-10 Because of its wide industrial implementation, researchers have studied the evaporation of droplets of different fluids including water, <sup>11–21</sup> ethanol, <sup>22–27</sup> hexane, <sup>10,28,29</sup> and dodecane <sup>27,30</sup> for more than a century. Droplet evaporation is typically characterized by the rate at which liquid is transformed into vapor. Many studies have been performed to investigate the evaporation rate of droplets residing on surfaces. 7,17,31-36 These studies typically depend on measuring the temporal size changes of a droplet and are limited by the transient effects occurring outside and/or inside the droplet such as interfacial dynamics at the liquid-vapor interface and contact line motion. Furthermore, microscale droplet evaporation dynamics ( $R < 500 \mu m$ , where R is the droplet radius of curvature) are difficult to characterize because of the changing shape of the droplet as the contact line shrinks and the droplet approaches the size of wettability heterogeneity on the surface. 40-42 In addition, most low surface tension liquids (<30 mN/m) exhibit low apparent receding contact angles ( $\theta_{\rm R}$  < 90°) on substrates. Studying evaporation of low surface tension droplets, which are typically volatile in ambient conditions, 43,44 remains a challenge.

Recently, we developed a steady method to investigate droplet evaporation of water by feeding microscale droplets ( $\approx$ 20  $\mu$ m in diameter) to a steady larger evaporating droplet. <sup>45</sup> By tuning the frequency of the dispensing microdroplets, the rate of evaporation was balanced with the rate of liquid addition, thereby maintaining a constant shape and size of the evaporating droplet. The evaporation rate was calculated from the volumetric flow rate of added liquid, eliminating spurious transient effects, and enabling the study of droplets having different sizes and shapes.

In this study, we employ this steady method to overcome the challenges facing low surface tension fluids by studying the evaporation of ethanol, hexane, and dodecane droplets having base radii 90  $\leq R_{\rm b} \leq$  400  $\mu{\rm m}$  and substrate temperatures 10 <  $T_{\rm s} <$  25 °C. We focus our work on a droplet size range where Marangoni and buoyant flows can be neglected, with droplet conduction and vapor-side mass-transfer governing evapora-

Received: August 2, 2020 Revised: September 25, 2020 Published: November 9, 2020





tion. We first validated our method by studying water droplet evaporation at different substrate temperatures, substrate wettabilities, and droplet sizes to ensure that the results and trends are consistent with previous well-validated works. Following validation, we utilized the steady method to study the evaporation of low surface tension fluid droplets. Our results show that the rate of droplet evaporation in the presence of noncondensable gases (NCGs) increases linearly with increasing  $R_b$  because of the linear dependence of contact line length. Furthermore, we demonstrate that surface functionality (i.e., nonwetting or wetting) becomes invariant during the evaporation of water droplets at elevated substrate temperatures  $(T_s > 45 \, ^{\circ}\text{C})$  because of the delicate balance formed between mass transfer at the droplet liquid-vapor interface and conduction heat transfer within the droplet. The outcomes of this work demonstrate the steady method as a powerful experimental platform for evaporation characterization of both microscale droplets and a variety of relevant working fluids.

#### **EXPERIMENTAL METHODS**

**Surface Fabrication, Functionalization, and Characterization.** For all evaporation experiments, we used functional surfaces having distinct wetting characteristics. Samples included polished silicon (Si) wafers and superhydrophobic microstructured copper oxide (CuO) surfaces functionalized with a hydrophobic self-assembled monolayer (SAM). For surface fabrication, functionalization, and characterization, please refer to Section S1 of the Supporting Information as well as previous work.

To enable the study of the effect of vanishing contact angle hysteresis, we used lubricant-infused surfaces (LISs) as well as hierarchically structured surfaces. Recent studies have shown fluorinated lubricants to be ideal for creating nonwetting surfaces applicable for low surface tension fluids. 46,47 To fabricate the LIS surfaces, the fabricated superhydrophobic microstructured CuO surfaces 48,49 functionalized with a hydrophobic SAM were infused with a fluorinated lubricant Fomblin Y14/6 (Section S1, Supporting Information). Superhydrophobic hierarchical surfaces were fabricated through spray coating of a stainless steel substrate with fluorinated silica (F–SiO<sub>2</sub>) particles. Fluorinated silica (F–SiO<sub>2</sub>) particles were suspended in *n*-hexane solution and spray-coated on a polyurethane-coated stainless-steel surface. The surface was then allowed to dry at room temperature for a day. Subsequently, the substrate was rinsed in hexane and then deionized (DI) water to remove excess F–SiO<sub>2</sub> particles.

**Experimental Procedure.** The working fluids studied were DI water (CAS 7732-18-5, Sigma-Aldrich), ethanol (CAS 64-17-5, Sigma-Aldrich), hexane (CAS 110-54-3, Sigma-Aldrich), and dodecane (CAS 112-40-3, Sigma-Aldrich). Table 1 summarizes the properties of the working fluids.

To study the effects of droplet size, surface temperature, relative humidity, and fluid volatility, we used six different substrates including Au-coated Si wafer (Si–Au), smooth Si wafer coated with a hydrophobic SAM (Si-HTMS), superhydrophobic CuO (CuO-HTMS), CuO LIS (F14/6), polished Cu (Cu), and a superhydrophobic hierarchical stainless-steel surface spray coated with fluorinated  ${\rm SiO}_2$  (FS) nanoparticles. The wetting characteristics of the substrates are summarized in Table 2. All the samples were square slabs having 25 mm side lengths with 0.5 mm thickness. Droplets having low apparent advancing contact angles approaching complete wetting (<10°) were not studied here because of the requirement for wide angle imaging techniques.

The experimental setup is described in detail in previous work. <sup>45</sup> Briefly, the experiment consists of a high-speed camera (FASTCAM SA2, Photron) integrated with a piezoelectric micro-goniometer (MCA-3, Kyowa Interface Science, Figure 1). <sup>45</sup> The rate of microdroplet addition (f) from the piezoelectric dispenser is governed

Table 1. Physical Properties of the Working Fluids at STP ( $T = 297 \text{ K}, \phi = 50\%, P = 1 \text{ atm}$ )

variable	symbol	water	ethanol	hexane	dodecane
liquid density [kg/m³]	$ ho_{ m f}$	998	789	655	750
vapor density [kg/m³]	$ ho_{ m v}$	0.76	1.91	3.564	7.11
liquid dynamic viscosity [mPa·s]	$\mu_{\mathrm{f}}$	0.9	1.1	0.3	1.34
vapor dynamic viscosity [mPa·s]	$\mu_{ m v}$	0.009	0.009	0.006	0.005
molecular weight [kg/kmol]	M	18.015	46.07	86.177	170.33
liquid-vapor surface tension [mN/m]	Γ	72	22	18.43	25.35
boiling point [°C]	$T_{\mathrm{b}}$	100	78.4	68.7	216
vapor pressure [kPa]	$P_{\infty}$	2.99	7.39	19.31	0.014
latent heat of vaporization [kJ/kg]	$h_{ m fg}$	2540	913.61	367	362.83
liquid thermal conductivity [W/(m·K)]	$k_{ m f}$	0.61	0.167	0.13	0.14
liquid specific heat [J/(kg·K)]	$C_{p,f}$	4184	2460	2260	2210
vapor specific heat [J/(kg·K)]	$C_{p,v}$	1996	1602	1655	1750
diffusion coefficient of vapor in air [mm²/s]	$D_{ m va}$	25.3	12	8	4.8
Lewis number	Le	1.15	1.9	1.5	3.5

Table 2. Wetting Characteristics of the Studied Fluids<sup>a</sup>

sample	$ heta_{ ext{a}}$ [°]	$ heta_{ ext{r}}  [^{\circ}]$	$\Delta  heta \ [^{\circ}]$				
Water							
Si-Au	$45.1 \pm 5.2$	0	$45.1 \pm 5.2$				
$Cu^X$	$85.0 \pm 1.9$	$35.1 \pm 15.2$	$49.9 \pm 15.7$				
Si-HTMS	$110.6 \pm 2.8$	$101.3 \pm 6.8$	$9.3 \pm 7.2$				
F14/6 <sup>X</sup>	$117.2 \pm 1.7$	$115.1 \pm 2.1$	$2.1 \pm 2.2$				
CuO-HTMS	$162.0 \pm 2.9$	$150.3 \pm 4.4$	$11.7 \pm 4.9$				
$FS^X$	$159.0 \pm 2.3$	$144.0 \pm 2.4$	$15.0 \pm 2.7$				
	Ethanol						
Cu	$32.0 \pm 3.9$	$23.1 \pm 3.2$	$8.9 \pm 4.2$				
F14/6	$70.0 \pm 2.6$	$67.1 \pm 3.2$	$2.9 \pm 3.4$				
FS	$93.0 \pm 2.7$	$68.1 \pm 5.6$	$24.9 \pm 6.2$				
Hexane							
F14/6	$43.4 \pm 2.4$	$40.1 \pm 3.2$	$3.3 \pm 3.4$				
Dodecane							
F14/6	$63.0 \pm 1.1$	$60.3 \pm 2.2$	$2.7 \pm 2.4$				

<sup>a</sup>The superscript X denotes not reported for evaporation for the corresponding working fluids.

by the frequency controller. The experiments were performed at a potential of 6-7 V, f=5-500 Hz, and sample-dispenser spacing of  $h\approx 6$  mm. Imaging was carried out at  $7-24\times$  magnification depending on the droplet size, and image acquisition was done at 200 frames per second. To control the sample surface temperature ( $10~^{\circ}\text{C} < T_s < 60~^{\circ}\text{C}$ ), we interfaced a temperature-controlled bath (PolyScience AD20R-30-V11BR,  $-30~^{\circ}\text{C} < T < 200~^{\circ}\text{C}$ ) with the stage. A handheld thermocouple device (4015, Traceable Products) was used to measure the sample surface temperatures, which differed from the set point chiller temperatures because of the contact resistance between the sample and stage. Similarly, the ambient temperature and relative humidity were measured and recorded using a handheld device (HX93BD, Omega). A mist humidifier (TaoTronics TT-

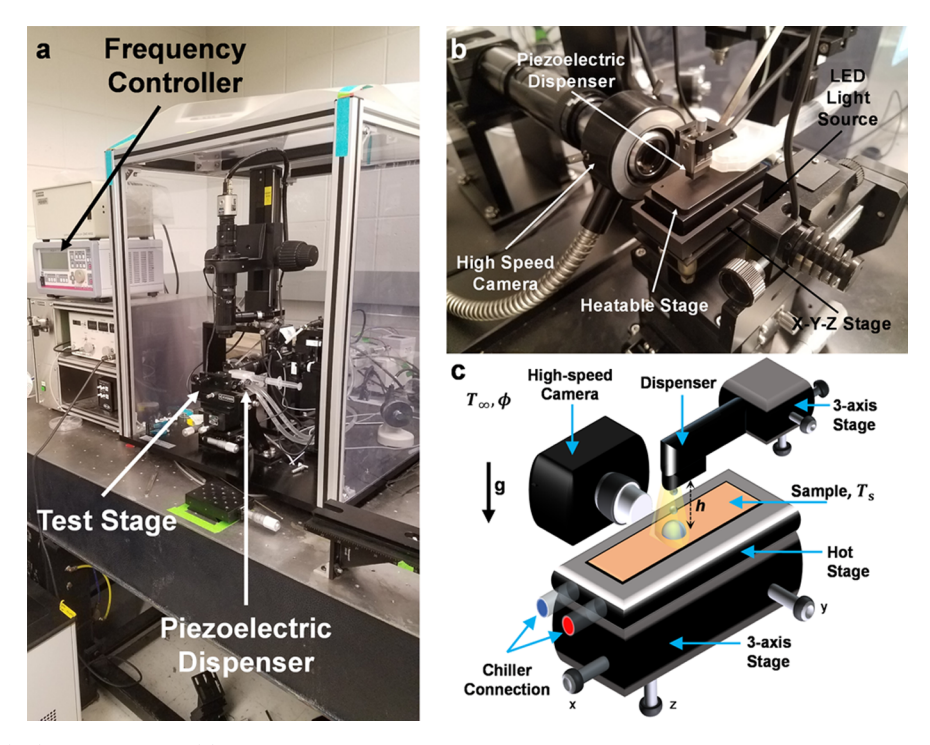


Figure 1. Photograph (a,b) and schematic (c) of the experimental setup. The temperature-controlled stage is connected to a chiller to control the surface temperature. The stage and the dispenser are connected to two independent 3-axis stages to maintain spatial control. A high-speed camera is integrated with the system to perform image analysis.

AH001) was connected to the system to control the relative humidity (20% <  $\phi$  < 60%).

The piezoelectric dispenser dispensed small ( $\approx$ 20  $\mu$ m), monodisperse droplets of the studied fluids (water, ethanol, hexane, dodecane) onto the sample surface, resulting in a single, larger droplet, on which we analyzed the evaporation dynamics. The evaporating droplet was brought into steady state by modulating the frequency (f) of microdroplet deposition. The droplet attaining a fixed size at a given f indicates steady state, where the rate of evaporation is equal to the rate of liquid deposition. The volumetric rate of liquid deposition can be calculated by multiplying the known deposition frequency at steady state (f) with the measured volume of the individual dispensed microdroplets (V), which equates to fV. Droplet volume analysis was performed using the mean size of the deposited microdroplets ( $R = 8.77 \pm 0.56 \,\mu\mathrm{m}$  for water,  $R = 16.47 \pm$ 1.73  $\mu$ m for ethanol, R = 12.67  $\pm$  0.22  $\mu$ m for hexane, and R = 5.37  $\pm$ 0.57 µm for dodecane) obtained by strobe imaging (Figure S1, Supporting Information). Table S3 summarizes the uncertainties associated with the different measurements during the experiments.

#### ■ RESULTS AND DISCUSSION

**Droplet Size.** Evaporation from a liquid—vapor interface greatly depends on the droplet size. S2,53 Previous works have shown a linear dependence of water droplet mass evaporation rate  $(\dot{m})$  as a function of increasing droplet base radius  $(R_{\rm b})$  at ambient temperature. Here, we initiated our experiments by studying the dependency  $\dot{m}$  on  $R_{\rm b}$  for different substrate temperatures  $(T_{\rm s}\approx 30,\,40,\,50\,^{\circ}{\rm C})$  with water, as shown in Figure 2. Though the dependence of  $\dot{m}$  on  $R_{\rm b}$  was linear, the apparent contact angle of the droplet played an important role. At lower substrate temperatures (closer to ambient),  $\dot{m}$  increased with higher hydrophobicity of the sample for similar-sized droplets (Figure 2a,b). The higher  $\dot{m}$  was due to the larger liquid—vapor surface area, which results in higher heat transfer with the gaseous environment when temperature differences between the droplet and substrate are small

(limited conduction from the substrate).<sup>20</sup> However, Figure 2c shows that  $\dot{m}$  is invariant with the apparent contact angle at higher  $T_{st}$  showing similar  $\dot{m}$  for droplets of similar size evaporating on different surfaces. The results indicate that a balance exists between the liquid-vapor mass-transfer resistance, which is lower for nonwetting samples because of increased liquid-vapor surface area (Figure S6) and the droplet-surface conduction heat transfer resistance, which is lower for hydrophilic surfaces because of lower conduction length scales. Here, the liquid-vapor interfacial area is considered for a fixed droplet radius of curvature (Figure S6). At elevated surface temperatures, the invariance to wetting points to the increasing limitation of heat conduction through the droplet to the evaporating interface (decreasing masstransfer resistance), making the contact line dominant in terms of evaporation dynamics because of its proximity to the substrate. It is important to note that the experiments conducted here were all done in the high thermal conductivity limit for the substrate. 54,55 The materials of choice included Cu, Si wafers, and stainless steel (SS), with intrinsic thermal conductivities of  $k_s = 400 \text{ W/(m·K)}$ , 150 W/(m·K), and 15 W/(m·K), respectively. Although the SS substrate (only used for ethanol experiments) had a lower thermal conductivity, it was much higher than the thermal conductivity of ethanol (Table 1). Furthermore, the added thermal resistance due to air pockets in the Cassie-Baxter state was negligible because of relatively low thermal resistance between the droplet and the substrate compared to vapor diffusion at the liquid-vapor interface and droplet conduction (Table 4, Section S4 of the Supporting Information).

In order to investigate the efficacy of the steady method on the evaporation dynamics of nonaqueous liquids, we studied the evaporation of ethanol, hexane, and dodecane droplets having 90 <  $R_{\rm b}$  < 400  $\mu$ m (Figure 3). In addition to differing

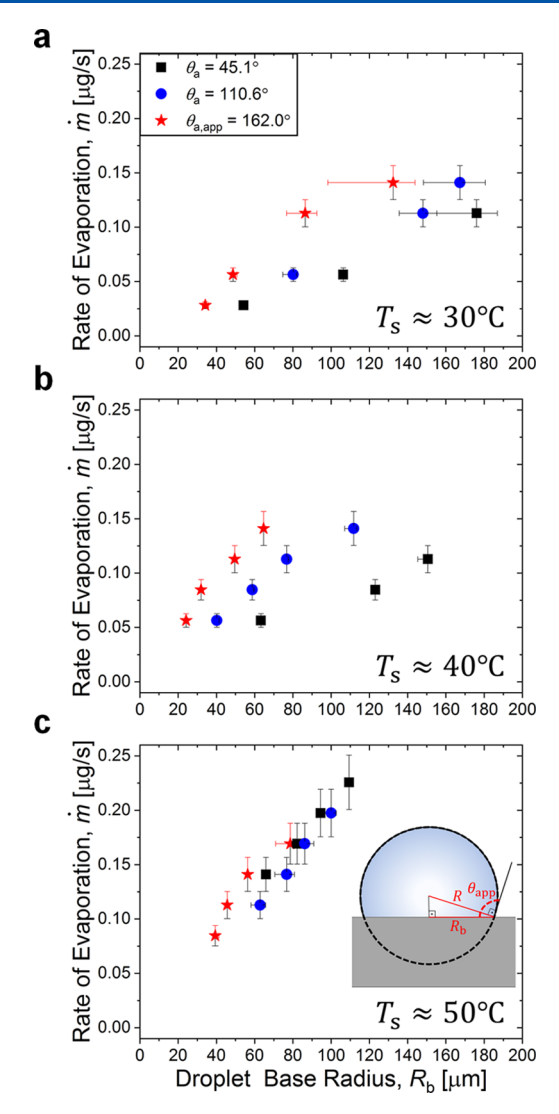


Figure 2. Droplet rate of evaporation as a function of droplet base radius for water droplets and tested samples [Si–Au ( $\theta_a \approx 45^\circ$ ), Si-TFTS ( $\theta_a \approx 111^\circ$ ), CuO-HTMS ( $\theta_{a,app} \approx 162^\circ$ )] for (a)  $T_s \approx 30$  °C, (b)  $T_s \approx 40$  °C, (c)  $T_s \approx 50$  °C. The rate of evaporation varies linearly with increasing droplet size because of the linear dependence of the contact line length with the base radius. It is seen that the slopes are increasing as the substrate temperatures are increased, and the contact angle loses its importance at elevated temperatures because of the balance between conduction within the droplet and interfacial transport with the surroundings (c). Superhydrophobic droplets were in the Cassie–Baxter state through the course of the experiments. Experiments were performed at standard room conditions ( $T_{\infty} = 25 \pm 0.5$  °C,  $\phi = 50\% \pm 5\%$ ).

surface tension, alcohols and hydrocarbons have significantly higher vapor pressures and lower boiling points as compared to water (Table 1). Hence, our evaporation experiments were limited to subambient temperatures (10 <  $T_{\rm s}$  < 25 °C). A close investigation of Figure 3 reveals that  $\dot{m}$  follows a linear trend with  $R_{\rm b}$  for ethanol, hexane, and dodecane, similar to that of water. To explore and understand the dynamics of evaporation on the studied fluids, we now investigate the driving forces for heat and mass transfer through scaling and thermal resistance analyses.

**External Natural Convection.** Natural convection has been shown to play an important role on droplet evaporation because of its effects on the vapor flow field. <sup>36,57</sup> To explore

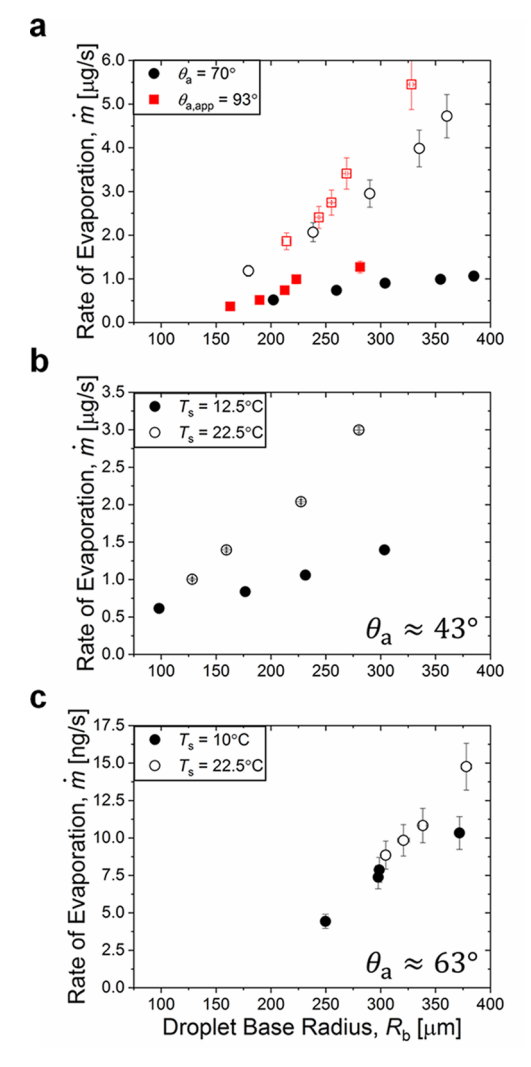


Figure 3. Droplet rate of evaporation as a function of droplet base radius for (a) ethanol on F14/6 ( $\theta_a\approx70^\circ$ ) and FS ( $\theta_{\rm a,app}\approx93^\circ$ , Wenzel state) for  $T_s\approx10$  °C (solid symbols) and  $T_s\approx22.5$  °C (hollow symbols), (b) hexane on F14/6 ( $\theta_a\approx43.4^\circ$ ) for  $T_s\approx12.5$  °C (solid symbols) and  $T_s\approx22.5$  °C (hollow symbols), and (c) dodecane on F14/6 ( $\theta_a\approx63.0^\circ$ ) for  $T_s\approx10$  °C (solid symbols) and  $T_s\approx22.5$  °C (hollow symbols). Experiments were performed at ambient conditions of (a)  $T_\infty=24.7\pm0.2$  °C,  $\phi=38\%\pm1\%$ , (b)  $T_\infty=23.7\pm0.5$  °C,  $\phi=25.1\%\pm0.9\%$ , and (c) of  $T_\infty=23.7\pm0.6$  °C,  $\phi=22.5\%\pm0.8\%$ .

the effects of natural convection with the surroundings, we calculate the Rayleigh number (Ra) of the heated sample and droplet, given by  $^{58}$ 

$$Ra = \frac{g\beta L_{\rm c}^{\ 3}\Delta T}{\alpha\nu} \tag{1}$$

where g is the gravitational constant,  $\beta$  is the thermal expansion coefficient of air,  $L_{\rm c}$  is the characteristic length of the heated horizontal surface or droplet,  $\Delta T$  is the temperature difference between the heated surface and ambient air or the ambient air and the evaporating droplet, and  $\alpha$  and  $\nu$  are the thermal diffusivity and kinematic viscosity of air, respectively. Note that two separate Rayleigh numbers were calculated. For the droplet, a temperature gradient is formed between the ambient air and droplet, in which case  $Ra \approx 2$  for the largest droplets considered ( $L_{\rm c} = A_{\rm s}/P \approx 800~\mu{\rm m}$ , where  $A_{\rm s}$  and P are the

surface area and perimeter of the droplet, respectively) and highest surface temperature ( $T_{\rm s}\approx 60~{\rm ^{\circ}C}$ ). The calculated  $Ra\approx 2$  is much smaller than the critical Rayleigh number for a heated horizontal surface ( $Ra\ll Ra_{\rm cr}=1708$ ). For the macroscopic flow governed by the length scale of the sample (natural convection from a heated horizontal surface),  $Ra\approx 850~(<Ra_{\rm cr}=1708)$  for  $L_{\rm c}=A_{\rm s}/P\approx 6.25$  mm, where  $A_{\rm s}$  and P are the surface area and perimeter of the sample in which the droplet resides on and  $T_{\rm s}\approx 60~{\rm ^{\circ}C}$ . Therefore, heat transport with the surroundings was governed by heat conduction for the experiments conducted here.

**Internal Droplet Natural Convection.** To explore the effects of internal natural convection, we calculated the Grashof number (Gr) of the evaporating droplet (Gr = Ra/Pr), where Pr is the liquid Prandtl number and Ra is defined by eq 1). Here,  $L_c$  is affected by the shape of the droplet  $(L_c = V/A_w)$ , where  $A_w = \pi R_b^2$  is the liquid/solid wetted area). Hence, Cr was calculated separately for wetting and nonwetting droplets for each working fluid. Table 3 shows that the

Table 3. Grashof (Gr), Marangoni (Ma), and Bond (Bo) Numbers of the Working Fluids

working fluid	$\theta$ [°]	$D [\mu m]$	Gr	Ма	Во
	45	50	$1.7 \times 10^{-4}$	280	$4.5 \times 10^{-7}$
DI water		500	0.17	2800	$4.5 \times 10^{-5}$
	135	50	0.03	16400	$1.5 \times 10^{-5}$
		500	34.6	1640	$1.5 \times 10^{-3}$
ethanol	45	50	$5.8 \times 10^{-3}$	310	$4.3 \times 10^{-4}$
		500	5.8	3130	$4.3 \times 10^{-2}$
hexane	45	50	0.1	570	$1.4 \times 10^{-3}$
		500	99.8	5720	0.14
dodecane	45	50	$4.3 \times 10^{-3}$	470	$2.8 \times 10^{-4}$
		500	4.3	4750	$2.8 \times 10^{-2}$

calculated Gr values are much smaller than the critical Gr for internal natural convection ( $Gr \ll Gr_{\rm cr} \approx 2400$ ). Hence, internal droplet natural convection effects were not present in our experiments.

**Marangoni Effects.** Given the presence of temperature gradients across the droplet, the presence of Marangoni forces and flows could affect the internal and external flow fields. To investigate how temperature or concentration gradients inside the evaporating droplet affect the overall evaporation dynamics, Marangoni convection inside the droplet was analyzed. An analyzed for the quantify the effects of Marangoni flows, the thermal Marangoni number (eq 2) and Bond number (eq 3) need to be calculated for representative contact angle values ( $\theta = 45^{\circ}$  for wetting and  $\theta = 135^{\circ}$  for nonwetting) for the smallest and largest droplets of interest (R = 50 and  $R = 50^{\circ}$ ) and for the highest surface temperature ( $R = 60^{\circ}$ ).

$$Ma = \frac{L_c \Delta T \left| \frac{\mathrm{d}\sigma}{\mathrm{d}T} \right|}{\alpha \mu} \tag{2}$$

$$Bo = \frac{gL_c^2(\rho_l - \rho_g)}{\sigma} \tag{3}$$

where  $|d\sigma/dT|$  is the rate of change of liquid—vapor surface tension with respect to temperature and  $L_c = V/A_w$  is the characteristic length.

Table 3 shows that the Marangoni numbers are higher than the critical value (Ma > 80-100), <sup>64</sup> and Bond numbers are

sufficiently small ( $Bo \ll 1$ ), suggesting that the internal flow is Marangoni convection dominated for each case. However, previous studies have shown that for sufficiently small droplets, Marangoni convection cannot initiate because of rolling caused by the instabilities of the mass center because of heating from below and cooling from above. Scaling the characteristic velocities of Marangoni flows obtained from the Marangoni number Ma ( $U_{\rm Ma} \sim {\rm Id}\sigma/{\rm d}T|\Delta T/\mu$ ) and body rotation because of the deviation of the mass center of the droplet, which is obtained by a balance of viscous dissipation and the gained potential energy because of rolling ( $U_{\rm R} \sim 2\Delta \rho g(\sigma/\rho g)^{3/2}/\mu D$ ) with  $\Delta \rho \sim \rho \beta \Delta T$ , we find the critical droplet diameter for each working fluid at which Marangoni convection will become dominant of M

$$D \sim \frac{\sigma \beta \sqrt{\frac{\sigma}{\rho g}}}{\left|\frac{d\sigma}{dT}\right|} \tag{4}$$

Utilization of eq 4 yields  $D \sim 0.7$  mm for water,  $D \sim 1.3$  mm for ethanol,  $D \sim 3.5$  mm for hexane, and  $D \sim 1$  mm for dodecane, much larger than the droplets studied here (D=2R < 0.5 mm). Furthermore, it has been experimentally demonstrated that for water droplets, which are prone to contamination, Marangoni flows are suppressed by 100 times even for very low surface contamination levels ( $\sim 300$  molecules/ $\mu$ m²). 65,66 Considering contamination effects and the fact that our droplets are smaller than the critical diameter, Marangoni effects were negligible for the conditions used in this study.

**Concentration Effects.** The effects of the temperature gradient in the vapor flow surrounding the evaporating droplet are characterized by analyzing the Ludwig–Soret effect and Dufour effect for the mixtures (i.e., air—water vapor, air—ethanol vapor, air-hexane vapor, and air—dodecane vapor). The Soret  $[S_T = -\nabla c/(c(1-c)\nabla T)]$  and the Dufour  $(D_T = (T_0 a^2/c_p \beta^2)(\partial \mu/\partial c)]$  numbers were calculated for each case and found to be negligible  $(S_T \approx 0.05, D_T \approx 0)$ . Hence, secondary effects due to the concentration gradients were negligible for our experiments.

**Evaporative Cooling.** Self-cooling of evaporating droplets can play an important role in the dynamics of evaporation.  $^{8,9}$  The conversion of liquid to vapor from the liquid—vapor interface of an evaporating droplet absorbs latent heat of vaporization ( $h_{\rm fg}$ ) from the remaining liquid in the droplet, which cools the droplet interface and in turn reduces the local liquid temperature, vapor pressure, and hence the evaporation rate. Self-cooling becomes especially important for nonwetting substrates because of the larger liquid—vapor interfacial area and droplet conduction resistance from the base, leading to increased resistance to evaporation as the droplet self-cools.

A number of previous studies have analytically captured the effect of self-cooling of droplets because of evaporation, focusing on isothermal interfaces. <sup>69,70</sup> For droplets evaporating in quiescent air, the liquid—vapor interfacial temperature can be calculated by a balance of the instantaneous rate of sensible heat transfer to the droplet and the instantaneous rate of heat absorption by the droplet in the absence of radiation as <sup>69</sup>

$$T_{\rm int} = T_{\infty} - \frac{h_{\rm fg} D_{\rm va} M P_{\rm v,int}}{k_f \overline{R} T_{\infty}}$$
 (5)

where  $D_{va}$  is the diffusion coefficient of the vapor (subscript v) in air (subscript a), M is the molecular mass of the evaporating

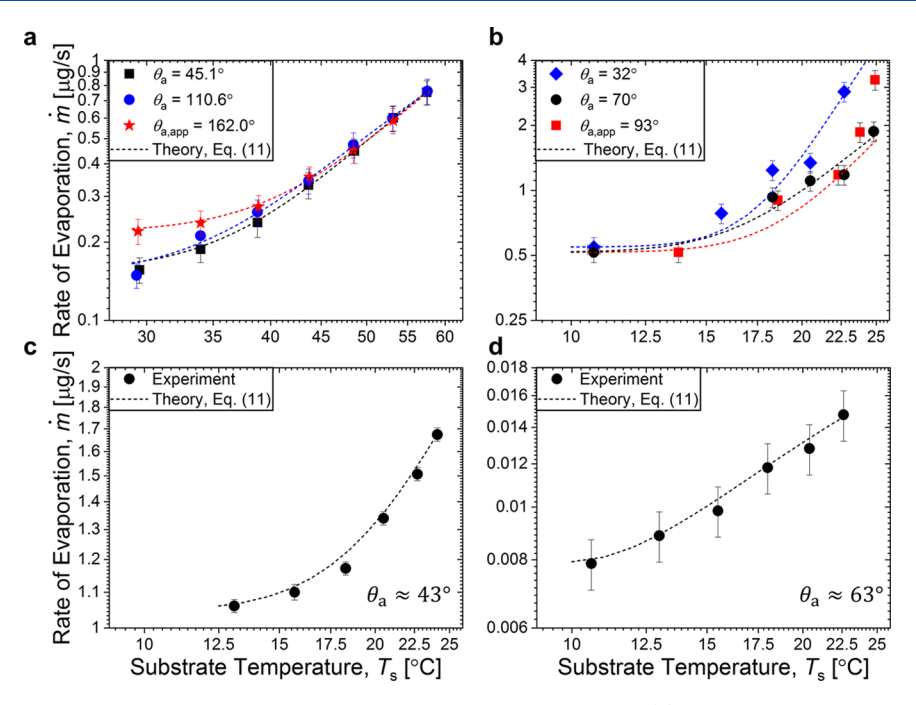


Figure 4. Droplet rate of evaporation as a function of the substrate temperature for fixed radii. (a) Rate of evaporation as a function of the substrate temperature for water droplets evaporating with  $R \approx 250~\mu \text{m}$  ( $T_{\infty} = 24.0 \pm 0.7~^{\circ}\text{C}$ ,  $\phi = 35.1\% \pm 1.3\%$ ), (b) rate of evaporation as a function of the substrate temperature for ethanol droplets evaporating with  $R \approx 200~\mu \text{m}$  ( $T_{\infty} = 24.7 \pm 0.2~^{\circ}\text{C}$ ,  $\phi = 38\% \pm 1\%$ ), (c) rate of evaporation as a function of the substrate temperature for hexane droplets evaporating with  $R \approx 300~\mu \text{m}$  ( $T_{\infty} = 23.7 \pm 0.5~^{\circ}\text{C}$ ,  $\phi = 25.1\% \pm 0.9\%$ ), (d) rate of evaporation as a function of the substrate temperature for dodecane droplets evaporating with  $R \approx 350~\mu \text{m}$  ( $T_{\infty} = 23.7 \pm 0.6~^{\circ}\text{C}$ ,  $\phi = 22.5\% \pm 0.8\%$ ). The same exponential trends were observed in all cases because of the dependence of evaporation on the vapor pressure and concentration. Fits were obtained by fitting eq 11 to the rate of evaporation data using the respective physical constants for each working fluid. The coefficients of determination (R-square) were >0.99 for water, hexane, and dodecane and >0.90 for ethanol. All experiments were performed on the same day for each working fluid to minimize the effects of the variations in ambient conditions.

Table 4. Thermal Resistance Analysis for Water, Ethanol, Hexane, and Dodecane at Different Surface Temperatures

Water									
		$T_{\rm s} \approx 30~^{\circ}{\rm C}$					$T_{\rm s} \approx 60~^{\circ}{\rm C}$		
θ [°]	R [μm]	$R_{th,\mathrm{base}}^*$	$R_{ m th,drop}^*$	$R_{ m th,int}^*$	R <sub>tot</sub> [K/W]	$R_{ m th,base}^*$	$R_{ m th,drop}^*$	$R_{ m th,int}^*$	R <sub>tot</sub> [K/W]
45	275	≪1	0.132	0.868	4058	≪1	0.222	0.778	2410
110	225	≪1	0.266	0.734	4570	≪1	0.438	0.562	2775
162	250	0.004	0.613	0.384	7750	0.004	0.740	0.255	6420
Ethanol									
	$T_s \approx 12.5  ^{\circ}\mathrm{C}$					$T_{\rm s} \approx 22.5~^{\circ}{\rm C}$			
θ [°]	R [μm]	R*,base	$R_{ m th,drop}^*$	$R_{ m th,int}^*$	R <sub>tot</sub> [K/W]	R*,base	$R_{ m th,drop}^*$	$R^*_{ m th,int}$	$R_{\rm tot} [{\rm K/W}]$
70	200	≪1	0.483	0.516	7140	≪1	0.560	0.439	6160
93	200	≪1	0.229	0.771	4620	≪1	0.251	0.749	4210
Hexane									
		$T_{\rm s} \approx 12.5$ °C	;				$T_{\rm s} \approx 22.5~^{\circ}{\rm C}$		
θ [°]	R [μm]	$R^*_{ ext{th,base}}$	$R_{ m th,drop}^*$	$R^*_{ m th,int}$	R <sub>tot</sub> [K/W]	$R_{ ext{th,base}}^*$	$R_{ m th,drop}^*$	$R_{ m th,int}^*$	$R_{\rm tot} [{\rm K/W}]$
43.4	350	≪1	0.461	0.538	4180	≪1	0.462	0.537	4170
					Dodecane				
		$T_{\rm s} \approx 12.5$ °C					$T_{\rm s} \approx 22.5~^{\circ}{\rm C}$		
θ [°]	R [μm]	$R^*_{ m th,base}$	$R_{ m th,drop}^*$	$R_{ m th,int}^*$	R <sub>tot</sub> [K/W]	$R_{ m th,base}^*$	$R_{ m th,drop}^*$	$R_{ m th,int}^*$	R <sub>tot</sub> [K/W]
63	400	≪1	0.826	0.173	2120	≪1	0.809	0.190	2170
<sup>a</sup> The * den	<sup>a</sup> The * denotes normalization by the total resistance value $(R_{tot})$ .								

liquid,  $P_{\text{v,int}}$  is the vapor pressure at the liquid—vapor interface temperature,  $k_{\text{f}}$  is the thermal conductivity of the evaporating liquid,  $\overline{R}$  is the universal gas constant, and  $T_{\infty}$  is the ambient air temperature. Equation 5 reveals that for given fluid and ambient conditions, the only unknown parameter is the

liquid—vapor interfacial temperature  $T_{\rm int}$ , which is solved iteratively. Here, it should be noted that the effects of the substrate on temperature have been neglected, which may not always hold true depending on the evaporation conditions. The effect of the substrate has already been extensively studied

for evaporating quasisteady droplets in the conduction dominated regime. <sup>71,72</sup> For such droplets, the nondimensional temperature distribution at the solid—liquid interface can be obtained by a balance of the energy conducted into the droplet from the substrate and energy transferred to the cooler liquid—vapor interface by conduction within the droplet <sup>71</sup>

$$\frac{T_{\rm s} - T_{\rm s,0}}{T_{\rm s} - T_{\infty}} \approx \sqrt{\frac{2k_{\rm f}}{k_{\rm s}}} \tag{6}$$

where  $T_s$  represents the bulk substrate temperature far from the liquid–solid interface,  $T_{s,0}$  represents the temperature at the center of the droplet solid–liquid interface, and  $k_s$  represents the thermal conductivity of the solid. Utilizing eq 6 for the working fluids and the substrates of interest  $(k_{\rm f} \sim 0.1~{\rm W/(m\cdot K)}, k_{\rm s} \sim 100~{\rm W/(m\cdot K)}, k_{\rm f}/k_{\rm s} \ll 1)$ , we observe  $(T_{\rm s} - T_{\rm s,0})/T_{\rm s} - T_{\infty} \approx 0$  and  $T_{\rm s} \approx T_{\rm s,0}$ . Hence, the scaling argument shows that the solid–liquid interface is isothermal and eq 5 is valid

Using eq 5, for water at room temperature ( $T_{\infty} = 24$  °C),  $\varphi = 50\%$  relative humidity, and atmospheric pressure (101 kPa), we calculated  $T_{\rm int} = 22.8$  °C, showing a 1.2 °C decrease in ambient conditions. More importantly, under the same environmental conditions, we calculated  $T_{\rm int} = 17.5$  °C for ethanol,  $T_{\rm int} = 14$  °C for hexane, and  $T_{\rm int} = 23.8$  °C for dodecane (Section S4, Supporting Information). The results indicate that self-cooling is important for hexane and ethanol and negligible for water and dodecane. The observed trend is expected because of the higher vapor pressures of hexane and ethanol, which enhances liquid-to-vapor mass transfer.

Effects of Surface Temperature and Droplet Mor**phology.** To study the effect of surface temperature  $(T_s)$ , the rate of evaporation  $(\dot{m})$  of similar-sized (<10% variation in droplet diameter) water droplets on varying samples was analyzed (Figure 4a). The results show an exponential dependence of  $\dot{m}$  on  $T_s$ . Furthermore, droplets evaporating at lower  $T_s$  are more sensitive to droplet shape (apparent contact angle) because of the relative imbalance between the thermal resistances associated with conduction within the droplet and mass transfer at the liquid-vapor interface. To quantify the effect of different mechanisms of heat and mass transfer, we use a thermal resistance analogy. Assuming spherical-cap droplet shapes ( $Bo \ll 1$ , Figure S2), we calculate the thermal resistance to heat transfer from the substrate to the droplet base (R<sub>th,base</sub>, Section S4, Supporting Information), thermal resistance to heat conduction within the droplet  $(R_{\rm th,drop} \approx \theta/4\pi R k_{\rm f} \sin \theta)$ , <sup>73</sup> and thermal resistance at the liquid-vapor interface  $(R_{\rm th,int})$ , Section S4, Supporting Information). The results of the analysis are given in Table 4 for all working fluids at the two temperature extremes. From Table 4, it can be concluded that droplet evaporation is governed by interfacial effects (vapor diffusion and conduction with the surroundings) and conduction within the droplet when Marangoni and natural convection effects are negligible. In addition, because the substrate has very low thermal resistance when compared to other thermal resistances ( $R_{\text{th,base}}^*$ ≪ 1, see Table 4 and Section S4 of the Supporting Information), we assume that the droplet base is at the same temperature as the substrate underneath it. Furthermore, droplet conduction resistance increases while interfacial resistance decreases as the surface becomes nonwetting (hydrophobic) because of morphological effects. As the contact angle increases, for similar radii droplets, overall

height of the droplet goes up, increasing the distance that the heat from the substrate must travel to reach the evaporating interface, effectively reflected as an increase in the droplet conduction resistance. In parallel, as the contact angle increases, the liquid-vapor interfacial area also increases, effectively increasing the total heat and mass transfer with the surroundings (reflected as decreased interfacial resistance). This, together with the higher conduction resistance, implies that the average temperature of the droplets will decrease as the surface becomes nonwetting because of lower heat conduction from the higher temperature substrate to the evaporating interface undergoing self-cooling. Our experimental observations here are in-line with results from previous numerical studies. 19 However, the average temperature of droplets on wetting (hydrophilic) surfaces will be higher because self-cooling effects are negligible because of effective conduction within the droplet. Hence, while the superhydrophobic droplet will have an almost constant temperature difference with the surroundings  $(T_{avg} \approx T_{int}, \Delta T = T_{avg} - T_{\infty},$ where  $T_{\text{int}}$  is limited by the wet-bulb temperature  $T_{\text{wb}}$ ), the hydrophilic droplet will have higher temperature difference with the surroundings  $(T_{\rm avg} \approx 0.5 (T_{\rm int} + T_{\rm s}), \Delta T = T_{\rm avg} - T_{\infty},$  where  $T_{\rm int}$  is limited by the wet-bulb temperature  $T_{\rm wb}$ ). At higher temperature differences between the sample surface and the droplet ( $\Delta T = T_s - T_{avg}$ ), higher temperature gradients within the droplet are formed, resulting in increased heat conduction through the droplet, effectively increasing its average temperature. Although this results in better diffusion because of decreased interfacial resistance, self-cooling effects become negligible for the superhydrophobic droplet because more heat is transferred through conduction. Simultaneously, mass transport through the interface becomes easier for the wetting droplet because of decreased interfacial resistance at elevated temperatures ( $T_s > 45$  °C). Hence, surface functionality and droplet morphology lose importance at elevated temperatures ( $T_s > 45$  °C) because of the formed balance between droplet conduction and interfacial effects for all studied water droplets (Figures 2c and 4a).

To further validate our hypothesis that droplet evaporation is governed by mass diffusion at the interface and droplet conduction, we expanded our studies to the evaporation of ethanol, hexane, and dodecane droplets (Figure 4b,d). Similar to water,  $\dot{m}$  increased exponentially as a function of  $T_s$  for each fluid even though the studied temperatures and the temperature ranges were much smaller (10 °C <  $T_s$  < 25 °C). The effects of apparent advancing contact angle could not be studied because of the difficulty in obtaining nonwetting droplet morphologies for low-surface tension working fluids. The quantitative results for ethanol, hexane, and dodecane matched with the water droplet results, lending credence for the need of a more rigorous scaling analysis examining the driving forces for evaporation.

Considering liquid and gas thermal conductivities and droplet morphology to be temperature independent for small-temperature variations, the droplet conduction heat-transfer resistance can be assumed to be independent of  $T_{\rm s}$  or  $T_{\infty}$ . Hence, the change in droplet evaporation behavior with changing  $T_{\rm s}$  is governed by vapor diffusion in the vicinity of the liquid—vapor interface (wetting droplet limit), which is governed by Fick's law of diffusion in the ambient air adjacent to the interface: <sup>74</sup>

$$J = D_{\rm va} \frac{\mathrm{d}c}{\mathrm{d}x} \sim \left(\frac{D_{\rm va}}{t}\right) (c - c_{\infty}) \tag{7}$$

where  $D_{\rm va}$  is the diffusion coefficient of vapor (subscript v) in air (subscript a) (Table 1), t is the thickness of the diffusion boundary layer, c is the vapor concentration at the liquid–vapor interface, and  $c_{\infty}$  is the concentration of vapor in the ambient air far from the droplet at the mass-transfer boundary layer edge. Note that although interfacial transport at the liquid–vapor interface is a key resistance to mass transfer from liquid to vapor, it is negligible compared to diffusional resistances encountered in NCG-laden environments and not considered here. <sup>45,75</sup> Assuming that water vapor at ambient conditions behaves as an ideal gas<sup>76</sup>

$$J(T_{\rm int}) = D_{\rm va} \frac{\mathrm{d}c}{\mathrm{d}x} \sim \frac{D_{\rm va}(P_{\rm v} - P_{\rm v,\infty})}{R_{\rm v}tT_{\rm int}} \sim \frac{P_{\rm v}(T_{\rm int})}{T_{\rm int}}$$
(8)

where  $R_{\rm v}$  is the specific gas constant for the evaporating liquid,  $P_{\rm v}$  is the vapor pressure of the evaporating fluid at the liquid–vapor interface, and  $P_{\rm v,\infty}$  is the vapor pressure of the evaporating fluid in ambient air far from the droplet. Using the Clausius–Clapeyron solution for an ideal gas, we obtain  $^{77}$ 

$$\ln\left(\frac{P_{\rm v}}{P_{\rm v,\infty}}\right) = \frac{h_{\rm fg}}{R_{\rm v}} \left(\frac{1}{T_{\infty}} - \frac{1}{T_{\rm int}}\right) \tag{9}$$

$$P_{\rm v}(T) = P_{\rm v,\infty} \exp\left(\frac{h_{\rm fg}}{R_{\rm v} T_{\rm \infty}}\right) \exp\left(-\frac{h_{\rm fg}}{R_{\rm v} T_{\rm int}}\right) \sim \exp\left(-\frac{h_{\rm fg}}{R_{\rm v} T_{\rm int}}\right)$$
(10)

Substituting eqs 10 into 8, we obtain an analytical relation for J as a function of  $T_{\rm int}$ 

$$J(T_{\rm int}) \sim \frac{P_{\rm v}(T_{\rm int})}{T_{\rm int}} \sim \frac{1}{T_{\rm int}} \exp\left(-\frac{h_{\rm fg}}{R_{\rm v}T_{\rm int}}\right)$$
(11)

Note that because  $T_{\rm int}$  is related to  $T_{\rm s}$ , we use  $T_{\rm s}$  on our experimental trend lines (Figure 4). Although high fidelity models incorporating contact angle and droplet shape effects have been developed for water droplet evaporation in gas diffusion-limited settings, few models exist that can accurately predict the evaporation of arbitrary low surface tension fluids. Hence, we have limited our analysis to the results of the scaling analysis as given by eq 11. Our experimental results (Figure 4) follow the trend obtained by eq 11 closely for higher temperatures, indicating the validity of the scaling analysis used to predict evaporation behavior by the steady method for different temperatures as well as elucidating the dynamics of liquid—vapor transport at the interface for droplets on different functional surfaces.

It is important to note that the surface temperature may also play a role in rate of evaporation by affecting the apparent contact angles of the formed droplets on surfaces. Careful analysis of the experimental results indicated no significant changes for droplets of any liquid used because of the negligible changes in the surface tension values over the studied temperature range (Figure S3, Supporting Information). A summary of the governing phenomena for water droplet evaporation for different temperatures and droplet morphologies is given in Table 5.

**Saturation State.** Another important phenomenon governing mass transport is the relative humidity, which represents the saturation state of a vapor in the ambient

Table 5. Phenomena Governing Water Droplet Evaporation  $^a$ 

$\theta$ [°]	$T_{\rm s}$ < $\approx$ 45 °C	$T_{\rm s}$ > $\approx$ 45 $^{\circ}$ C
≪90°	vapor diffusion	balanced
≈90°	vapor diffusion	balanced
≫90°	droplet conduction	balanced

"For low-to-intermediate temperatures, droplet evaporation is governed by vapor diffusion effects at the liquid—vapor interface for wetting droplets and by droplet conduction for nonwetting droplets. At intermediate-to-high temperatures, a balance between effective vapor diffusion and droplet conduction is formed because of higher average droplet temperatures, yielding more heat to conduct from the base and negligible self-cooling effects for all droplet morphologies.

environment. Relative humidity is physically represented by a ratio of vapor pressures, which can be described by concentrations considering ideal gas behavior<sup>76</sup>

$$\phi = \frac{P_{v,\infty}}{P_{v,\infty}^*} \sim \frac{c_{\infty}}{c_{\infty}^*} \tag{12}$$

where the superscript \* represents the equilibrium states at a given temperature. Revisiting Fick's Law (eq 7)

$$J \sim \frac{D_{\text{va}}}{t} (c - c_{\infty}) \sim -c_{\infty}^* \phi \tag{13}$$

Our experiments show a linear decrease in the rate of evaporation with increasing  $\phi$  (Figure S4, Supporting Information). As  $\phi$  increases, the surrounding air approaches saturation and the equilibrium state, diminishing mass transport. Because of the negligible concentration of vapors of the low surface tension fluids in air, the evaporation dynamics of ethanol, hexane, and dodecane were independent on the air relative humidity, as shown in Figure S5, Supporting Information.

Vapor Pressure. Volatility of a liquid is measured by the equilibrium vapor pressure generated by the liquid at a fixed temperature (Table 1). Liquids having higher vapor pressure are more volatile, as they are closer to the boiling point, and more liquid is transferred into the vapor phase because of larger concentration gradients between the liquid—vapor interface of the droplet and the ambient air. Figure 5 shows the effect of vapor pressure on the rate of evaporation for the obtained exponential fits of the studied fluids (hexane, ethanol, water, and dodecane). The results show that the rate of evaporation significantly increases for a given surface temperature as the volatility increases.

In summary, we present a rigorous analysis of droplet evaporation of fluids having distinct properties using the developed steady method.<sup>45</sup> Low surface tension liquids tend to wet conventional hydrophobic surfaces because the surfaces and the low surface tension liquids usually have comparable surface energy values. The liquid droplets thus easily spread on such surfaces, causing wetting and larger liquid-surface contact area. This necessitates the need to have larger imaging apertures for studying evaporation, which can lead to higher uncertainties in the evaporation measurements. Most low surface tension fluids are also highly volatile and rapidly evaporate and are thus difficult to study because of the short evaporation timescales. Moreover, it is difficult to dispense similar-sized discrete droplets of low surface tension liquids continuously because the liquid wets the dispensing nozzle/ needle, often forming a film around the tip. Using the steady

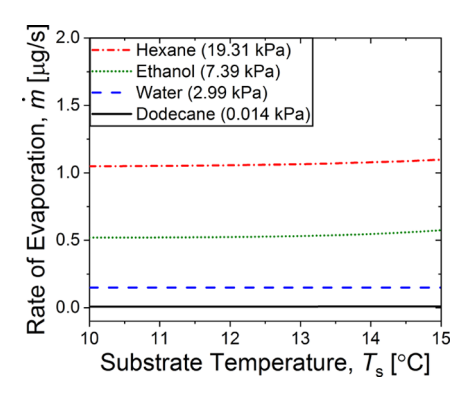


**Figure 5.** Rate of evaporation as a function of substrate temperature for fluids of different volatilities. At a given temperature, hexane is the most volatile (characterized by higher vapor pressure), which also shows the highest evaporation rate because of higher concentration gradients. Dodecane is the least volatile, showing the lowest evaporative behavior because of lower concentration gradients. Fits were obtained from experimental data and the exponential behavior the evaporation rate displays with surface temperature.

method, we show that it is possible to accurately characterize the evaporation dynamics of droplets of volatile fluids because of the ability to control droplet deposition timescales (i.e., modulation of the frequency of deposition) to match the fast evaporation timescales. Furthermore, size control of evaporating liquids has traditionally been difficult to achieve, leading to studies with larger droplets. This issue was predominant for the volatile fluids, which may be toxic and pose health risks to the researcher. Because the steady method allows for the study of droplets having small length scales ( $D \sim 100 \ \mu m$ ) because of the ability to dispense microdroplets ( $D \sim 10 \, \mu \text{m}$ ), the amount of the fluid that is used is minimized. Using minimal fluid makes the method not only more advantageous because of the ability to analyze smaller droplets (fewer gravity effects) but also much safer than traditional methods where the dispensed volumes of potentially toxic fluids are much higher.

Another advantage of the steady method is its high-throughput functionality. Multiple droplet sizes and conditions can be characterized in a single experimental run without removing the liquid from the surface. This has implications for the study of a multitude of phenomena related to phase change and interfacial science, for example, binary droplet systems, where two droplets could be printed and their impact on the evaporation behavior on one another could be analyzed. In addition, similar methods with the same experimental setup have already been used to explore cloaking on LISs, <sup>78</sup> induced coalescence, <sup>79,80</sup> droplet jumping, <sup>51,81,82</sup> and fluid mechanics. <sup>83</sup>

The steady method also enables the spatial control of monodisperse microdroplet deposition. For biphilic or hybrid surfaces, droplets can precisely be deposited to study evaporation dynamics.<sup>84</sup> Although we only considered flat surfaces here, the steady technique also enables the study of evaporation on microscale wires.

Because of the adaptability of the steady method, many interesting interfacial and phase change phenomena can be studied in the future. One interesting study would be to measure the thermal conductivity of fluids via time-domain thermoreflectance, where the droplet size could be fixed by using the steady method. It would also be interesting to study other fluids that may not evaporate quickly but that can undergo phase change in the droplet after deposition such as freezing on a supercooled substrates, liquid metal drop-

lets, <sup>87,88</sup> and phase change of paraffins because of heat loss to the substrate. <sup>89</sup> Furthermore, the effects of wetting state (Cassie-Baxter, Wenzel, or during Cassie-Baxter to Wenzel transition) for droplets evaporating on textured structures can be further investigated. In addition, because of the high resolution in dispensing droplets, contact line phenomena such as droplet sliding can be accurately characterized.

#### CONCLUSIONS

In this study, evaporation dynamics of water droplets were investigated using the steady method for a wide range of droplet base radii (20–400  $\mu$ m) on different surfaces having a wide range of wettability characteristics ( $32^{\circ} < \theta_a < 162^{\circ}$ ). In addition, employing the steady method, microdroplets of different low surface tension fluids (ethanol, hexane, and dodecane) were also studied to characterize their evaporation rates in ambient conditions. Because the steady method enables the decoupling of physical phenomena that are simultaneously governing the droplet evaporation process such as surface temperature, relative humidity, and volatility, we individually studied each phenomenon to observe their respective contribution to evaporation dynamics. Our results showed that the rate of evaporation has a linear dependence on the droplet base radius for each tested surface temperature and working fluid. We also show that for a given surface, an exponential dependence exists between the droplet rate of evaporation and the surface temperature, and that the wettability characteristics of the surface loses its role on the evaporation dynamics at higher surface temperatures. We also noted an inverse linear trend between the rate of evaporation and relative humidity for water droplets and found no effect of relative humidity on the rate of evaporation for the droplets of low surface tension fluids. Increases in the rate of evaporation values for more volatile fluids were also observed because of elevated liquid-to-vapor mass transfer caused by higher vapor pressures. This work sheds light on the evaporation dynamics of microdroplets of diverse working fluids on different surfaces and offers insights into alternate avenues in the study of droplet evaporation of different shapes and sizes.

## ASSOCIATED CONTENT

#### Supporting Information

The Supporting Information is available free of charge at https://pubs.acs.org/doi/10.1021/acs.langmuir.0c02272.

Surface fabrication, functionalization, and characterization; strobe images for monodisperse droplets; detailed calculation of the interfacial temperatures; plots of contact angle variations; thermal resistance analyses; effects of relative humidity; variation of the interfacial surface area with droplet contact angle; and uncertainty associated with experiments (PDF)

#### AUTHOR INFORMATION

## **Corresponding Authors**

A. Alperen Günay — Department of Mechanical Science and Engineering, University of Illinois at Urbana Champaign, Urbana, Illinois 61801, United States; orcid.org/0000-0002-2013-9101; Email: gunay@photon.t.u-tokyo.ac.jp

Nenad Miljkovic — Department of Mechanical Science and Engineering and Department of Electrical and Computer Engineering, University of Illinois at Urbana⊠Champaign, Urbana, Illinois 61801, United States; Materials Research Laboratory, University of Illinois, Urbana, Illinois 61801, United States; International Institute for Carbon Neutral Energy Research (WPI-I2CNER), Kyushu University, Fukuoka 819-0395, Japan; ocid.org/0000-0002-0866-3680; Email: nmiljkov@illinois.edu

#### **Authors**

- Marisa Gnadt Department of Mechanical Science and Engineering, University of Illinois at Urbana⊠Champaign, Urbana, Illinois 61801, United States
- Soumyadip Sett Department of Mechanical Science and Engineering, University of Illinois at Urbana⊠Champaign, Urbana, Illinois 61801, United States
- Hamed Vahabi Department of Biomedical Engineering, Duke University, Durham, North Carolina 27708, United States
- Arun K. Kota Department of Mechanical and Aerospace Engineering, North Carolina State University, Raleigh, North Carolina 27695, United States; orcid.org/0000-0001-9061-7896

Complete contact information is available at: https://pubs.acs.org/10.1021/acs.langmuir.0c02272

#### **Author Contributions**

A.A.G. and N.M. conceived the initial idea for this study. N.M. guided the work. A.A.G. and M.G. fabricated, functionalized, and characterized the functional samples and carried out the experiments. H.V and A.K.K fabricated and functionalized the stainless steel-based omniphobic sample. S.S. fabricated, functionalized, and characterized the LISs. A.A.G., M.G., and S.S. analyzed the data. All authors contributed to the writing of the manuscript and have given approval to the final version of this manuscript.

#### Notes

The authors declare no competing financial interest.

#### ACKNOWLEDGMENTS

The authors gratefully acknowledge the funding support from the National Science Foundation under award no. 1554249. N.M. gratefully acknowledges the funding support from the International Institute for Carbon Neutral Energy Research (WPI–I2CNER), sponsored by the Japanese Ministry of Education, Culture, Sports, Science and Technology. A.K.K. gratefully acknowledges the support from the American Chemical Society Petroleum Research Fund and from the National Science Foundation under award 1751628.

#### REFERENCES

- (1) Abramzon, B.; Sirignano, W. A. Droplet vaporization model for spray combustion calculations. *Int. J. Heat Mass Transfer* **1989**, 32, 1605–1618.
- (2) Crespo, A.; LiÑAn, A. Unsteady Effects in Droplet Evaporation and Combustion AU CRESPO, A. Combust. Sci. Technol. 1975, 11, 9–18.
- (3) Sazhin, S. S.; Abdelghaffar, W. A.; Sazhina, E. M.; Heikal, M. R. Models for droplet transient heating: Effects on droplet evaporation, ignition, and break-up. *Int. J. Therm. Sci.* **2005**, *44*, 610–622.
- (4) Kitano, T.; Nishio, J.; Kurose, R.; Komori, S. Evaporation and combustion of multicomponent fuel droplets. *Fuel* **2014**, *136*, 219–225.
- (5) Boreyko, J. B.; Collier, C. P. Delayed Frost Growth on Jumping-Drop Superhydrophobic Surfaces. ACS Nano 2013, 7, 1618–1627.

- (6) Duan, F.; Ward, C. A. Investigation of Local Evaporation Flux and Vapor-Phase Pressure at an Evaporative Droplet Interface. *Langmuir* **2009**, *25*, 7424–7431.
- (7) Hu, H.; Larson, R. G. Evaporation of a Sessile Droplet on a Substrate. *J. Phys. Chem. B* **2002**, *106*, 1334–1344.
- (8) Pan, Z.; Weibel, J. A.; Garimella, S. V. Influence of Surface Wettability on Transport Mechanisms Governing Water Droplet Evaporation. *Langmuir* **2014**, *30*, 9726–9730.
- (9) Dash, S.; Garimella, S. V. Droplet Evaporation Dynamics on a Superhydrophobic Surface with Negligible Hysteresis. *Langmuir* **2013**, 29, 10785–10795.
- (10) Shahidzadeh-Bonn, N.; Rafaï, S.; Azouni, A.; Bonn, D. Evaporating droplets. *J. Fluid Mech.* **2006**, 549, 307–313.
- (11) Camp, D.; Sadler, J. E.; Busscher, W. J. A Water Droplet Evaporation and Temperature Model. *Trans. ASAE* **1989**, *32*, 0457–0462.
- (12) Kulinich, S. A.; Farzaneh, M. Effect of contact angle hysteresis on water droplet evaporation from super-hydrophobic surfaces. *Appl. Surf. Sci.* **2009**, *255*, 4056–4060.
- (13) Xu, X.; Luo, J. Marangoni flow in an evaporating water droplet. *Appl. Phys. Lett.* **2007**, *91*, 124102.
- (14) Sobac, B.; Brutin, D. Thermal effects of the substrate on water droplet evaporation. *Phys. Rev. E: Stat., Nonlinear, Soft Matter Phys.* **2012**, *86*, 021602.
- (15) Tseng, C. C.; Viskanta, R. Enhancement of water droplet evaporation by radiation absorption. Fire Saf. J. 2006, 41, 236–247.
- (16) Ghasemi, H.; Ward, C. A. Energy Transport by Thermocapillary Convection during Sessile-Water-Droplet Evaporation. *Phys. Rev. Lett.* **2010**, *105*, 136102.
- (17) Gelderblom, H.; Marín, Á. G.; Nair, H.; van Houselt, A.; Lefferts, L.; Snoeijer, J. H.; Lohse, D. How water droplets evaporate on a superhydrophobic substrate. *Phys. Rev. E: Stat., Nonlinear, Soft Matter Phys.* **2011**, 83, 026306.
- (18) McHale, G.; Aqil, S.; Shirtcliffe, N. J.; Newton, M. I.; Erbil, H. Y. Analysis of Droplet Evaporation on a Superhydrophobic Surface. *Langmuir* **2005**, *21*, 11053–11060.
- (19) Pan, Z.; Dash, S.; Weibel, J. A.; Garimella, S. V. Assessment of water droplet evaporation mechanisms on hydrophobic and superhydrophobic substrates. *Langmuir* **2013**, *29*, 15831–15841.
- (20) Stauber, J. M.; Wilson, S. K.; Duffy, B. R.; Sefiane, K. Evaporation of Droplets on Strongly Hydrophobic Substrates. *Langmuir* **2015**, *31*, 3653–3660.
- (21) Debuisson, D.; Merlen, A.; Senez, V.; Arscott, S. Stick—Jump (SJ) Evaporation of Strongly Pinned Nanoliter Volume Sessile Water Droplets on Quick Drying, Micropatterned Surfaces. *Langmuir* **2016**, 32, 2679–2686.
- (22) Sefiane, K.; Tadrist, L.; Douglas, M. Experimental study of evaporating water—ethanol mixture sessile drop: influence of concentration. *Int. J. Heat Mass Transfer* **2003**, *46*, 4527–4534.
- (23) Sazhin, S. S.; Elwardany, A.; Krutitskii, P. A.; Castanet, G.; Lemoine, F.; Sazhina, E. M.; Heikal, M. R. A simplified model for bicomponent droplet heating and evaporation. *Int. J. Heat Mass Transfer* **2010**, 53, 4495–4505.
- (24) Sefiane, K.; Bennacer, R. Nanofluids droplets evaporation kinetics and wetting dynamics on rough heated substrates. *Adv. Colloid Interface Sci.* **2009**, *147*–*148*, 263–271.
- (25) Hallett, W. L. H.; Beauchamp-Kiss, S. Evaporation of single droplets of ethanol-fuel oil mixtures. *Fuel* **2010**, 89, 2496–2504.
- (26) Maqua, C.; Castanet, G.; Grisch, F.; Lemoine, F.; Kristyadi, T.; Sazhin, S. S. Monodisperse droplet heating and evaporation: Experimental study and modelling. *Int. J. Heat Mass Transfer* **2008**, *51*, 3932–3945.
- (27) Kristyadi, T.; Deprédurand, V.; Castanet, G.; Lemoine, F.; Sazhin, S. S.; Elwardany, A.; Sazhina, E. M.; Heikal, M. R. Monodisperse monocomponent fuel droplet heating and evaporation. *Fuel* **2010**, *89*, 3995–4001.
- (28) Poulard, C.; Bénichou, O.; Cazabat, A. M. Freely Receding Evaporating Droplets. *Langmuir* **2003**, *19*, 8828–8834.

- (29) Miller, R. S.; Harstad, K.; Bellan, J. Evaluation of equilibrium and non-equilibrium evaporation models for many-droplet gas-liquid flow simulations. *Int. J. Multiphase Flow* **1998**, 24, 1025–1055.
- (30) Rosner, D. E.; Chang, W. S. Transient Evaporation and Combustion of a Fuel Droplet Near Its Critical Temperature. *Combust. Sci. Technol.* **1973**, *7*, 145–158.
- (31) Picknett, R. G.; Bexon, R. The evaporation of sessile or pendant drops in still air. *J. Colloid Interface Sci.* **1977**, *61*, 336–350.
- (32) Nešić, S.; Vodnik, J. Kinetics of droplet evaporation. *Chem. Eng. Sci.* **1991**, *46*, 527–537.
- (33) Deegan, R. D.; Bakajin, O.; Dupont, T. F.; Huber, G.; Nagel, S. R.; Witten, T. A. Contact line deposits in an evaporating drop. *Phys. Rev. E: Stat. Phys., Plasmas, Fluids, Relat. Interdiscip. Top.* **2000**, *62*, 756–765.
- (34) Brutin, D.; Starov, V. Recent advances in droplet wetting and evaporation. *Chem. Soc. Rev.* **2018**, *47*, 558–585.
- (35) Ruiz, O. E.; Black, W. Z. Evaporation of water droplets placed on a heated horizontal surface. *J. Heat Transfer* **2002**, 124, 854–863.
- (36) Crafton, E. F.; Black, W. Z. Heat transfer and evaporation rates of small liquid droplets on heated horizontal surfaces. *Int. J. Heat Mass Tran.* **2004**, *47*, 1187–1200.
- (37) Gao, N.; Geyer, F.; Pilat, D. W.; Wooh, S.; Vollmer, D.; Butt, H.-J.; Berger, R. How drops start sliding over solid surfaces. *Nat. Phys.* **2018**, *14*, 191–196.
- (38) Butt, H.-J.; Gao, N.; Papadopoulos, P.; Steffen, W.; Kappl, M.; Berger, R. Energy Dissipation of Moving Drops on Superhydrophobic and Superoleophobic Surfaces. *Langmuir* **2017**, *33*, 107–116.
- (39) Gao, N.; Chiu, M.; Neto, C. Receding Contact Line Motion on Nanopatterned and Micropatterned Polymer Surfaces. *Langmuir* **2017**, 33, 12602–12608.
- (40) Diby, N. D.; Wang, J.; Duan, Y. Motion behaviour of water-droplet on alternate superhydrophobic/hydrophilic ZnO wetting-patterned surface. *Surf. Eng.* **2020**, *36*, 636–642.
- (41) Dai, X.; Yang, F.; Yang, R.; Huang, X.; Rigdon, W. A.; Li, X.; Li, C. Biphilic nanoporous surfaces enabled exceptional drag reduction and capillary evaporation enhancement. *Appl. Phys. Lett.* **2014**, *105*, 191611.
- (42) Dorrer, C.; Rühe, J. Mimicking the Stenocara Beetle—Dewetting of Drops from a Patterned Superhydrophobic Surface. *Langmuir* **2008**, *24*, 6154–6158.
- (43) Fukatani, Y.; Orejon, D.; Kita, Y.; Takata, Y.; Kim, J.; Sefiane, K. Effect of ambient temperature and relative humidity on interfacial temperature during early stages of drop evaporation. *Phys. Rev. E* **2016**, 93, 043103.
- (44) Kita, Y.; Okauchi, Y.; Fukatani, Y.; Orejon, D.; Kohno, M.; Takata, Y.; Sefiane, K. Quantifying vapor transfer into evaporating ethanol drops in a humid atmosphere. *Phys. Chem. Chem. Phys.* **2018**, 20, 19430–19440.
- (45) Günay, A. A.; Sett, S.; Oh, J.; Miljkovic, N. Steady Method for the Analysis of Evaporation Dynamics. *Langmuir* **2017**, *33*, 12007–12015.
- (46) Preston, D. J.; Lu, Z.; Song, Y.; Zhao, Y.; Wilke, K. L.; Antao, D. S.; Louis, M.; Wang, E. N. Heat Transfer Enhancement During Water and Hydrocarbon Condensation on Lubricant Infused Surfaces. Sci. Rep. 2018, 8, 540.
- (47) Sett, S.; Yan, X.; Barac, G.; Bolton, L. W.; Miljkovic, N. Lubricant-Infused Surfaces for Low-Surface-Tension Fluids: Promise versus Reality. *ACS Appl. Mater. Interfaces* **2017**, *9*, 36400–36408.
- (48) Enright, R.; Miljkovic, N.; Sprittles, J.; Nolan, K.; Mitchell, R.; Wang, E. N. How Coalescing Droplets Jump. ACS Nano 2014, 8, 10352–10362.
- (49) Nam, Y.; Ju, Y. S. A comparative study of the morphology and wetting characteristics of micro/nanostructured Cu surfaces for phase change heat transfer applications. *J. Adhes. Sci. Technol.* **2013**, 27, 2163–2176.
- (50) Cha, H.; Chun, J. M.; Sotelo, J.; Miljkovic, N. Focal Plane Shift Imaging for the Analysis of Dynamic Wetting Processes. *ACS Nano* **2016**, *10*, 8223–8232.

- (51) Yan, X.; Zhang, L.; Sett, S.; Feng, L.; Zhao, C.; Huang, Z.; Vahabi, H.; Kota, A. K.; Chen, F.; Miljkovic, N. Droplet Jumping: Effects of Droplet Size, Surface Structure, Pinning, and Liquid Properties. ACS Nano 2019, 13, 1309–1323.
- (52) Chen, X.; Ma, R.; Li, J.; Hao, C.; Guo, W.; Luk, B. L.; Li, S. C.; Yao, S.; Wang, Z. Evaporation of Droplets on Superhydrophobic Surfaces: Surface Roughness and Small Droplet Size Effects. *Phys. Rev. Lett.* **2012**, *109*, 116101.
- (53) Tsai, P.; Lammertink, R. G. H.; Wessling, M.; Lohse, D. Evaporation-Triggered Wetting Transition for Water Droplets upon Hydrophobic Microstructures. *Phys. Rev. Lett.* **2010**, *104*, 116102.
- (54) David, S.; Sefiane, K.; Tadrist, L. Experimental investigation of the effect of thermal properties of the substrate in the wetting and evaporation of sessile drops. *Colloids Surf., A* **2007**, 298, 108–114.
- (SS) Dunn, G. J.; Wilson, S. K.; Duffy, B. R.; David, S.; Sefiane, K. The strong influence of substrate conductivity on droplet evaporation. *J. Fluid Mech.* **2009**, *6*23, 329–351.
- (56) Hegseth, J. J.; Rashidnia, N.; Chai, A. Natural convection in droplet evaporation. *Phys. Rev. E: Stat. Phys., Plasmas, Fluids, Relat. Interdiscip. Top.* **1996**, *54*, 1640–1644.
- (57) Carle, F.; Sobac, B.; Brutin, D. Experimental evidence of the atmospheric convective transport contribution to sessile droplet evaporation. *Appl. Phys. Lett.* **2013**, *102*, 061603.
- (58) Bergman, T. L.; Incropera, F. P.; DeWitt, D. P.; Lavine, A. S. Fundamentals of Heat and Mass Transfer; John Wiley & Sons, 2011.
- (59) Koschmieder, E. L. Bénard Cells and Taylor Vortices; Cambridge University Press, 1993.
- (60) Kays, W. M. Convective Heat and Mass Transfer; Tata McGraw-Hill Education, 2012.
- (61) Lu, G.; Duan, Y.-Y.; Wang, X.-D.; Lee, D.-J. Internal flow in evaporating droplet on heated solid surface. *Int. J. Heat Mass Tran.* **2011**, *54*, 4437–4447.
- (62) Holman, J. P. Heat Transfer-Si Units-Sie; Tata McGraw-Hill Education, 2002.
- (63) Tam, D.; von ARNIM, V.; McKinley, G. H.; Hosoi, A. E. Marangoni convection in droplets on superhydrophobic surfaces. *J. Fluid Mech.* **2009**, *624*, 101–123.
- (64) Carey, V. P. Liquid Vapor Phase Change Phenomena: An Introduction to the Thermophysics of Vaporization and Condensation Processes in Heat Transfer Equipment; CRC Press, 2018.
- (65) Hu, H.; Larson, R. G. Analysis of the Effects of Marangoni Stresses on the Microflow in an Evaporating Sessile Droplet. *Langmuir* **2005**, *21*, 3972–3980.
- (66) Hu, H.; Larson, R. G. Marangoni Effect Reverses Coffee-Ring Depositions. J. Phys. Chem. B 2006, 110, 7090-7094.
- (67) Hort, W.; Linz, S. J.; Lücke, M. Onset of convection in binary gas mixtures: Role of the Dufour effect. *Phys. Rev. A: At., Mol., Opt. Phys.* **1992**, *45*, 3737.
- (68) Geelhoed, P.; Westerweel, J.; Kjelstrup, S.; Bedeaux, D. Thermophoresis. *Encyclopedia of Microfluidics and Nanofluidics*, 2015, pp3305–3309.
- (69) Erbil, H. Y.; Dogan, M. Determination of Diffusion Coefficient–Vapor Pressure Product of Some Liquids from Hanging Drop Evaporation. *Langmuir* **2000**, *16*, 9267–9273.
- (70) David, S.; Sefiane, K.; Tadrist, L. Experimental investigation of the effect of thermal properties of the substrate in the wetting and evaporation of sessile drops. *Colloids Surf.*, A **2007**, 298, 108–114.
- (71) Sadhal, S. S.; Plesset, M. S. Effect of solid properties and contact angle in dropwise condensation and evaporation. *J. Heat Tran.* **1979**, *101*, 48–54.
- (72) Tio, K.-K.; Sadhal, S. S. Thermal analysis of droplet spray evaporation from a heated solid surface. *J. Heat Tran.* **1992**, *114*, 220–226.
- (73) Miljkovic, N.; Enright, R.; Wang, E. N. Effect of droplet morphology on growth dynamics and heat transfer during condensation on superhydrophobic nanostructured surfaces. *ACS Nano* **2012**, *6*, 1776–1785.
- (74) Fick, A. Ueber Diffusion. Ann. Phys. 1855, 170, 59-86.

- (75) Chavan, S.; Cha, H.; Orejon, D.; Nawaz, K.; Singla, N.; Yeung, Y. F.; Park, D.; Kang, D. H.; Chang, Y.; Takata, Y.; Miljkovic, N. Heat Transfer through a Condensate Droplet on Hydrophobic and Nanostructured Superhydrophobic Surfaces. *Langmuir* **2016**, *32*, 7774–7787.
- (76) Moran, M. J.; Shapiro, H. N.; Boettner, D. D.; Bailey, M. B. Fundamentals of Engineering Thermodynamics; Wiley, 2010.
- (77) Kittel, C.; Kroemer, H.; Scott, H. L. Thermal Physics, 2nd ed. Am. J. Phys. 1998, 66, 164–167.
- (78) Günay, A. A.; Sett, S.; Ge, Q.; Zhang, T.; Miljkovic, N. Cloaking Dynamics on Lubricant-Infused Surfaces. *Adv. Mater. Interfaces* **2020**, 7 (19), 2000983.
- (79) Yan, X.; Feng, L.; Zhang, L.; Sett, S.; Li, L.; Miljkovic, N. "Dancing Droplets": Partial Coalescence on Superhydrophobic Surfaces. *J. Heat Transfer* **2020**, *142*, 030904.
- (80) Yan, X.; Chen, F.; Sett, S.; Chavan, S.; Li, H.; Feng, L.; Li, L.; Zhao, F.; Zhao, C.; Huang, Z.; Miljkovic, N. Hierarchical condensation. ACS Nano 2019, 13, 8169–8184.
- (81) Yan, X.; Huang, Z.; Sett, S.; Oh, J.; Cha, H.; Li, L.; Feng, L.; Wu, Y.; Zhao, C.; Orejon, D.; Chen, F.; Miljkovic, N. Atmosphere-mediated superhydrophobicity of rationally designed micro/nano-structured surfaces. *ACS Nano* **2019**, *13*, 4160–4173.
- (82) Yan, X.; Chen, F.; Zhang, X.; Qin, Y.; Zhao, C.; Sett, S.; Cha, H.; Hoque, M. J.; Zhao, F.; Huang, Z.; Miljkovic, N. Atmosphere-Mediated Scalable and Durable Biphilicity on Rationally Designed Structured Surfaces. *Adv. Mater. Interfaces* **2020**, *7*, 2000475.
- (83) Yan, X.; Sett, S.; Feng, L.; Zhang, L.; Huang, Z.; Chen, F.; Miljkovic, N. "Swimming Jellyfish": Visualizing Jet-Like Internal Flow in Coalescing Droplets. J. Heat Transfer 2019, 141, 100901.
- (84) Hoque, M. J.; Yan, X.; Keum, H.; Li, L.; Cha, H.; Park, J. k.; Kim, S.; Miljkovic, N. High-Throughput Stamping of Hybrid Functional Surfaces. *Langmuir* **2020**, *36*, 5730.
- (85) Cahill, D. Thermal Conductance of Solid-Solid and Solid-Liquid Interfaces, 2005.
- (86) Jung, S.; Tiwari, M. K.; Doan, N. V.; Poulikakos, D. Mechanism of supercooled droplet freezing on surfaces. *Nat. Commun.* **2012**, *3*, 615.
- (87) Yang, T.; Kwon, B.; Weisensee, P. B.; Kang, J. G.; Li, X.; Braun, P.; Miljkovic, N.; King, W. P. Millimeter-scale liquid metal droplet thermal switch. *Appl. Phys. Lett.* **2018**, *112*, 063505.
- (88) Yang, T.; Foulkes, T.; Kwon, B.; Kang, J. G.; Braun, P. V.; King, W. P.; Miljkovic, N. An Integrated Liquid Metal Thermal Switch for Active Thermal Management of Electronics. *IEEE Trans. Compon. Packag. Manuf. Technol.* **2019**, *9*, 2341–2351.
- (89) Chatterjee, R.; Beysens, D.; Anand, S. Delaying Ice and Frost Formation Using Phase-Switching Liquids. *Adv. Mater.* **2019**, *31*, 1807812.